

Thermoelectric properties of directionally grown $\text{Bi}_2\text{Ba}_2\text{Co}_2\text{O}_8/\text{Ag}$ composites: effect of annealing

Sh. Rasekh¹ · A. Sotelo¹ · M. A. Torres¹ · P. Bosque¹ · M. A. Madre¹ · J. C. Diez¹

Received: 9 May 2016 / Accepted: 25 July 2016 / Published online: 6 August 2016
© Springer Science+Business Media New York 2016

Abstract $\text{Bi}_2\text{Ba}_2\text{Co}_2\text{O}_8$ thermoelectric ceramics with Ag additions (0, 1, 3, and 5 wt%) have been successfully textured using the laser floating zone method. Microstructure has shown that samples are composed by thermoelectric grains, together with a high amount of secondary phases, and that 3 wt% Ag addition leads to the best grain orientation. These microstructural benefits have been reflected in the highest thermoelectric performances determined in these samples. It has also been found that annealing procedure leads to a drastic decrease of secondary phases amount and raises the oxygen content in the thermoelectric phase. These modifications are reflected in an important decrease of electrical resistivity, ρ (compared to the as-grown samples) without drastic modification of Seebeck coefficient, S . As a consequence, the highest thermoelectric performances, determined through the power factor, have been reached in the 3 wt% Ag textured and annealed samples in the whole measured temperature range. The maximum PF ($=S^2/\rho$) values at 650 °C determined in these samples are very close to the highest reported in single crystals or very low rate LFZ grown $\text{Bi}_2\text{Ba}_2\text{Co}_2\text{O}_8$ compounds, making them very attractive for practical applications.

1 Introduction

Thermoelectric (TE) materials are characterized by their ability to transform thermal to electrical energy through the Seebeck effect. As a consequence, they can increase the classical energy transforming systems efficiency by transforming the wasted heat into useful electricity. This higher efficiency is reflected in decreasing energy consumption, and reducing the CO_2 emissions.

The TE materials performance is quantified using the dimensionless Figure-of-Merit, $ZT = TS^2/\rho\kappa$, where T , S , ρ and κ are absolute temperature, Seebeck coefficient, electrical resistivity, and thermal conductivity, respectively [1]. In this expression, the electrical part (S^2/ρ) is called power factor, PF.

Nowadays, some practical applications of TE materials can be found in refrigeration, or waste heat harvesting in automobiles exhausts [2, 3]. Most of these applications are based on alloys and/or intermetallic TE materials, such as Bi_2Te_3 or CoSb_3 , with relatively high TE performances at low and intermediate temperatures. Their main drawbacks are possible oxidation and/or degradation at high temperatures under air, releasing toxic or heavy elements. These limitations have been overtaken by the discovery of large TE properties in Na_xCoO_2 compound [4], formed by relatively cheap and environmentally friendly materials, with high chemical stability at high temperatures under oxidizing environments. Consequently, many studies of CoO-based families have been performed in the last years [5–12]. Crystallographically, they can be described as an alternate stacking of a conducting CdI_2 -type CoO_2 layer with a two-dimensional triangular lattice and an insulating rock-salt-type (RS) where the rest of cations can be found. Both sublattices possess common a - and c -axis lattice parameters and β angles but different b -axis length,

✉ M. A. Madre
amadre@unizar.es

¹ Instituto de Ciencia de Materiales de Aragón (CSIC-Universidad de Zaragoza), M^a de Luna, 3, 50018 Zaragoza, Spain

producing a misfit along the b-direction [13]. The strong anisotropy of these systems makes necessary to produce bulk materials with a good grain alignment to achieve high TE properties. Some relevant techniques have been successfully used to induce a good grain orientation in several functional ceramic and ceramic–metal composite systems [14–26].

Other important factor directly influencing the TE properties of these materials is the electrical connectivity through the grain boundaries, which can be reflected in further decrease of their electrical resistivity. This improvement of grain boundaries has been already evidenced in similar ceramic systems which showed that it can be produced by metallic Ag additions, leading to a ceramic matrix–metal composite with improved electrical transport properties [27–32].

$\text{Bi}_2\text{Ba}_2\text{Co}_2\text{O}_8$ material has been chosen due to the small amount of work published on this compound, together with the previous results obtained in pure $\text{Bi}_2\text{Ba}_2\text{Co}_2\text{O}_8$ textured at very small rates [12, 33]. As a consequence, the objective of this work is producing high performances bulk $\text{Bi}_2\text{Ba}_2\text{Co}_2\text{O}_8$ textured materials using the LFZ technique at relatively high growth rates (30 mm/h), adding Ag to improve grains electrical connectivity, and trying to reach TE properties comparable to the obtained in very low rates grown materials.

2 Experimental

$\text{Bi}_2\text{Ba}_2\text{Co}_2\text{O}_8 + x \text{ wt}\% \text{ Ag}$ ($y = 0, 1, 3,$ and 5) polycrystalline ceramics were prepared from commercial $\text{Bi}(\text{NO}_3)_3 \cdot 5\text{H}_2\text{O}$ (16.9144 g, Aldrich, 98 %), BaCO_3 (14.6098 g, Panreac, 98 %), $\text{Co}(\text{NO}_3)_2 \cdot 6\text{H}_2\text{O}$ (5.5473 g, Panreac, 98 %), and metallic Ag (Aldrich, 99 %; 0, 0.3030, 0.9278, and 1.5790 g, for the 0, 1, 3, and 5 wt% Ag, respectively) compounds by a sol–gel method. The powders were weighed and dissolved in 200 ml mixture of HNO_3 (Panreac, analysis grade 60 %) and distilled water (with an approximate relationship of 50 vol% of each compound). To the obtained clear pink solution, citric acid (12 g, Panreac, 99.5 %), and ethyleneglycol (12 ml, Panreac, 99 %), were added. Solvent evaporation was slowly performed in order to decompose the nitric acid excess, which allows the polymerization reaction between ethyleneglycol and citric acid, producing the coordination compound with all the cations in form of a pink gel [34]. Once this gel has been totally dried, it is further heated at 350 °C until its decomposition by slow self combustion. The resulting fine powder was mechanically ground and calcined at 700 and 750 °C for 12 h, with an intermediate manual grinding. This step is of especial importance when texturing process is produced by the LFZ technique: it has

been designed to decompose BaCO_3 which, otherwise, would do it in the molten zone, disturbing the solidification front, and leading to grain misorientations. The so-obtained powders were cold isostatically pressed in form of cylinders (~ 120 mm long and 2–3 mm diameter) under around 200 MPa applied pressure for 1 min.

The green ceramic cylinders were subsequently used as feed in a LFZ texturing system successfully used in previous works [33]. All samples were grown at 30 mm/h, with a seed rotation of 3 rpm, in order to maintain the cylindrical geometry in the final textured material while the feed has been rotated at 15 rpm, in the opposite direction, to improve the mixture of cations in the molten zone and, consequently, its homogeneity. After the texturing process, long (more than 150 mm) cylindrical and geometrically homogeneous samples have been obtained. These textured materials were then cut into shorter pieces with the adequate sizes for their characterization (~ 15 mm long). Moreover, taking into account previous results in similar systems with incongruent melting [35] which show that annealing the as-grown textured materials drastically raises their thermoelectric performances [36], some of the samples were annealed at 750 °C for 24 h.

The main phases identification in all the textured samples was carried out using powder X-ray diffraction (XRD) in a Rigaku D/max-B X-ray powder diffractometer ($\text{CuK}\alpha$ radiation), between 5° and 60°. Microstructural observations were performed on longitudinal polished samples using a Field Emission Scanning Electron Microscope (FESEM, Carl Zeiss Merlin) fitted with an energy dispersive spectrometer (EDS). Micrographs of these samples have been recorded to analyze the different phases, their orientation and distribution.

Steady-state simultaneous measurements of resistivity and Seebeck coefficient were performed using the standard dc four-probe technique in a LSR-3 apparatus (Linseis GmbH) between 50 and 650 °C under he atmosphere. From these data, PF values as a function of temperature were calculated in order to evaluate the final samples TE performances.

3 Results and discussion

3.1 As-grown samples

Powder XRD patterns of the different as-grown $\text{Bi}_2\text{Ba}_2\text{Co}_2\text{O}_8 + x \text{ wt}\% \text{ Ag}$ composites are displayed (from 5 to 40° for clarity) in Fig. 1. As it can be clearly observed in the graph, most of the peaks correspond to the misfit cobaltite $\text{Bi}_2\text{Ba}_2\text{Co}_2\text{O}_8$ phase (indicated by their diffraction planes in Fig. 1a) [11]. On the other hand, the peak marked with a asterisk can be associated to a BiBaO_3 secondary

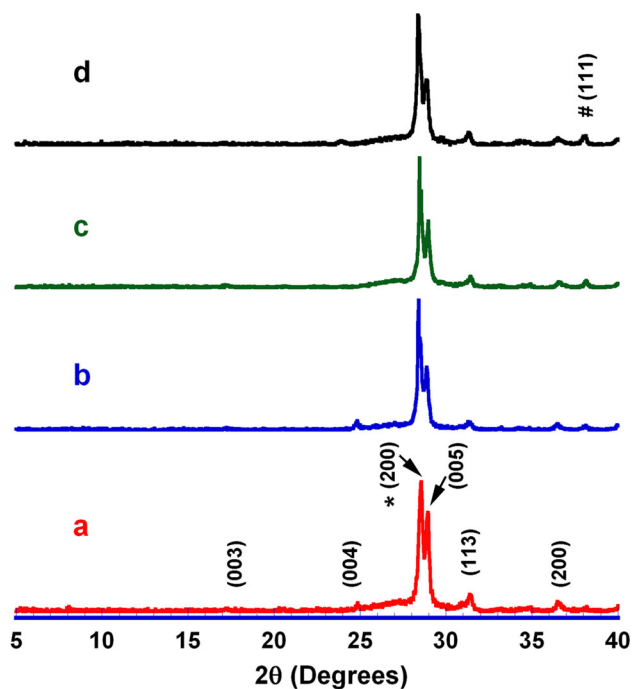


Fig. 1 Powder XRD diagrams for the as-grown $\text{Bi}_2\text{Ba}_2\text{Co}_2\text{O}_8$ textured samples, with *a* 0; *b* 1; *c* 3; and *d* 5 wt% Ag. Crystallographic planes have been indicated for the $\text{Bi}_2\text{Ba}_2\text{Co}_2\text{O}_8$ phase. Asterisk corresponds to a Bi–Ba–O solid solution while the hashtag indicates the metallic Ag

phase with P121/n1 space group [37], while the one shown by hashtag in Fig. 1d is identified as the (111) plane of metallic Ag [38]. This is a clear indication that Ag has been kept in metallic state, in agreement with previous works in a very similar compound which showed that no Ag is incorporated in the $\text{Bi}_2\text{Ca}_2\text{Co}_{1.8}\text{O}_8$ crystal structure [39]. Moreover, the secondary phase proportion is increased when Ag is added to the samples, as it can be deduced from its (200) peak higher relative intensity. This effect can be associated to two opposite factors modifying the molten zone due to the presence of Ag. Firstly, liquid Ag can reflect some fraction of the laser radiation leading to a lower incident power in the inner part of the rod, and secondly, due to the reported effect of Ag in decreasing the melting temperature in similar systems [27]. All these combined effects are drastically modifying the molten zone temperature, leading to radically different phase proportions from those produced in Ag-free samples.

The microstructural evolution of samples, as a function of Ag content, is illustrated in Fig. 2 where representative SEM micrographs, performed in polished longitudinal sections of all samples, are displayed. In these images, at a first sight it can be clearly seen that Ag-free samples possess a poor grain orientation, which seems to be increased with Ag addition until 3 wt%. Further Ag addition starts to produce an important grain misorientation. This grains

orientation evolution could be explained by the presence of an eutectic close to the $\text{Bi}_2\text{Ba}_2\text{Co}_2\text{O}_8 + 3 \text{ wt\% Ag}$ composition, which can lead to a good grain orientation as observed in other closely related systems [40].

Moreover, these micrographs show that all samples are mainly composed by three different contrasts (numbered in Fig. 2a for clarity). Additionally, another contrast appears in all Ag containing samples (#4 in Fig. 2c) and a new one only identified in 5 wt% Ag samples (#5 in Fig. 2d). All these contrasts have been associated through EDS analysis to different phases. Grey contrast (#1) corresponds to the $\text{Bi}_2\text{Ba}_2\text{Co}_2\text{O}_8$ phase, while dark and light grey (#2 and #3, respectively) ones, to BaCo_2O_z and $\text{Bi}_3\text{Ba}_2\text{O}_y$ approximate compositions. Contrast #4 appears in all Ag containing samples and it is difficult to be distinguished as it is very similar to contrast #1. It can be only identified by its rounded particle shape, and it has been associated to metallic Ag. Finally, very dark grey contrast (#5) has only been found in significant amounts in 5 wt% Ag samples and corresponds to BaO. On the other hand, when observing these micrographs, it seems that the proportion of light grey contrast ($\text{Bi}_3\text{Ba}_2\text{O}_y$) is relatively increased when Ag is added to the $\text{Bi}_2\text{Ba}_2\text{Co}_2\text{O}_8$ system, compared with the Ag-free samples. This observation is in agreement with the XRD data which showed that the amount of BiBaO_3 solid solution in the samples was increased when Ag was added. On the other hand, further observations have shown that 5 wt% Ag samples possess large Ag particles in the outer zone of the rods, as illustrated in Fig. 3. In this image, it can be easily seen that the region surrounding the Ag particle is mainly formed by secondary phases, clearly indicating a destabilization of the molten zone due to the large amount of Ag.

In order to determine the effect produced by these structural and microstructural features, electrical resistivity variation with temperature has been determined and displayed in Fig. 4 for all samples. As it can be easily observed in the graph, all samples possess semiconducting-like behaviour in the whole measured temperature range. Moreover, in spite of the higher amount of secondary phases found in the Ag containing samples, all of them possess lower resistivity values than the Ag-free ones. This result clearly indicates that, at least in this case, the grains alignment plays a more important role than the amount of secondary phases on the resulting electrical resistivity. Furthermore, the lowest measured electrical resistivity values in samples with 3 wt% Ag are in agreement with their best grain alignment already discussed in SEM section (see Fig. 2) and the presence of large Ag particles and the associated destabilization in the solidification front illustrated in Fig. 3. The lowest values determined in these samples at room temperature ($22 \text{ m}\Omega \text{ cm}$), are in the same order of the best previously reported ones for sintered

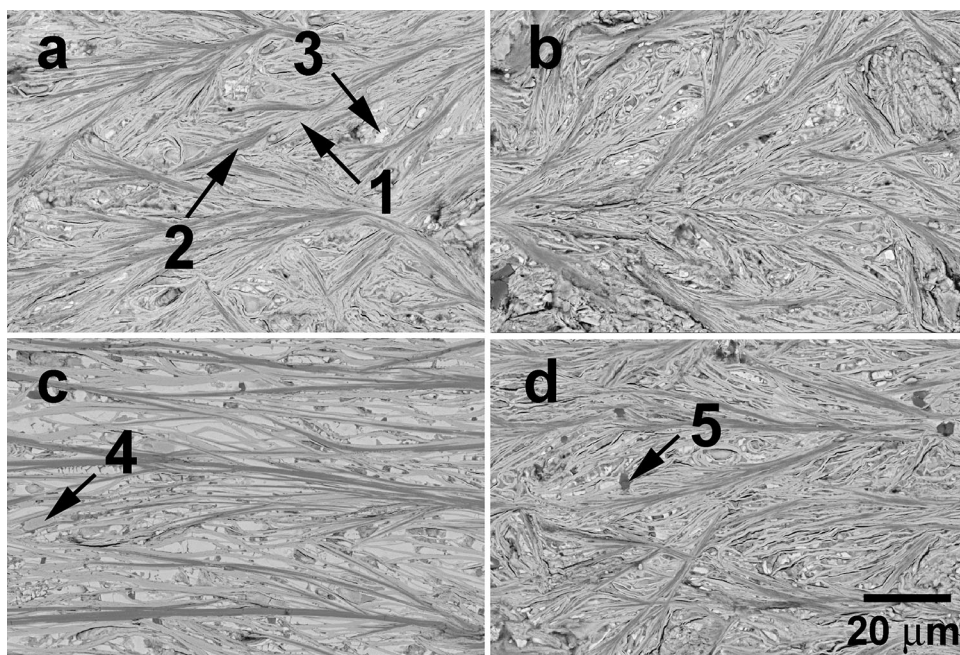


Fig. 2 Scanning electron micrographs from longitudinal polished as-grown $\text{Bi}_2\text{Ba}_2\text{Co}_2\text{O}_8$ samples with different Ag content: **a** 0; **b** 1; **c** 3; and **d** 5 wt%. The numbers indicate different phases: (#1) $\text{Bi}_2\text{Ba}_2\text{Co}_2\text{O}_8$; (#2) Ba–Co–O solid solution; (#3) Bi–Ba–O solid solution; (#4) metallic Ag; and (#5) BaO

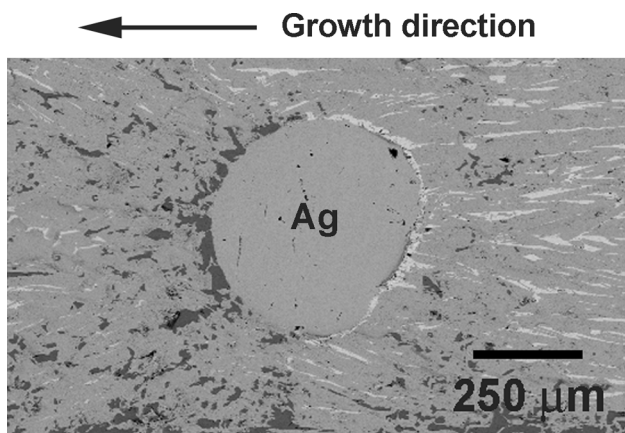


Fig. 3 FESEM close view image of a $\text{Bi}_2\text{Ba}_2\text{Co}_2\text{O}_8 + 5 \text{ wt\% Ag}$ sample performed in the external region of an as-grown rod, showing a large Ag particle

$\text{Bi}_2\text{Ba}_2\text{Co}_2\text{O}_8$ materials (pure and Ag-doped), which are typically between 550 and 21 $\text{m}\Omega \text{ cm}$ [11, 41–46]. Moreover, they are also comparable to the lowest reported values in textured $\text{Bi}_2\text{Ba}_2\text{Co}_2\text{O}_8$ materials, which are in the 10–250 $\text{m}\Omega \text{ cm}$ range [12, 33, 42, 47]. On the other hand, they are still far from the values reported in single crystals (4 $\text{m}\Omega \text{ cm}$) measured along the *ab* plane [48, 49].

When considering the high temperature (650 °C) values, they are clearly lower than the measured at room temperature, reaching the minimum ones in 3 wt% Ag samples (11 $\text{m}\Omega \text{ cm}$). These values are much lower than the ones

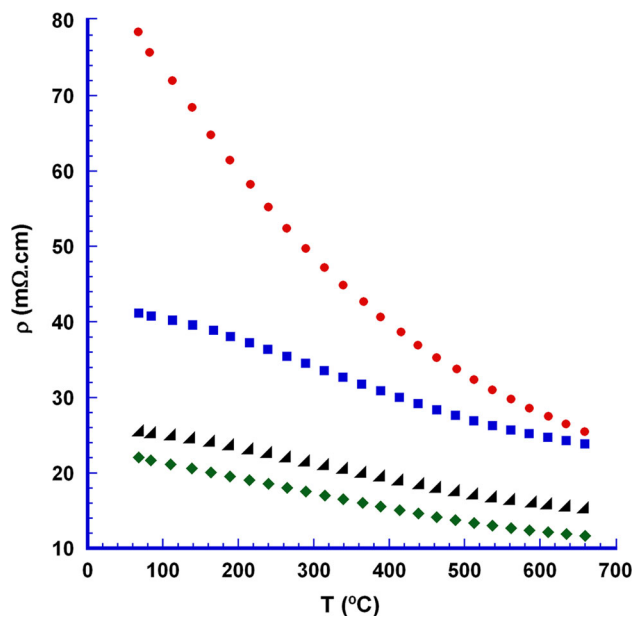


Fig. 4 Temperature dependence of the electrical resistivity for as-grown $\text{Bi}_2\text{Ba}_2\text{Co}_2\text{O}_8$ samples with different Ag content: circle 0; square 1; diamond 3; and lower right triangle 5 wt%

found in $\text{Bi}_2\text{Ba}_2\text{Co}_2\text{O}_8$ sintered materials (33 $\text{m}\Omega \text{ cm}$) [11, 43] and comparable with the obtained in $\text{Bi}_2\text{Ba}_2\text{Co}_2\text{O}_8$ textured samples (between 8.5 and 50 $\text{m}\Omega \text{ cm}$) [12, 33, 47].

Figure 5 displays the variation of Seebeck coefficient with temperature as a function of Ag content. As can be

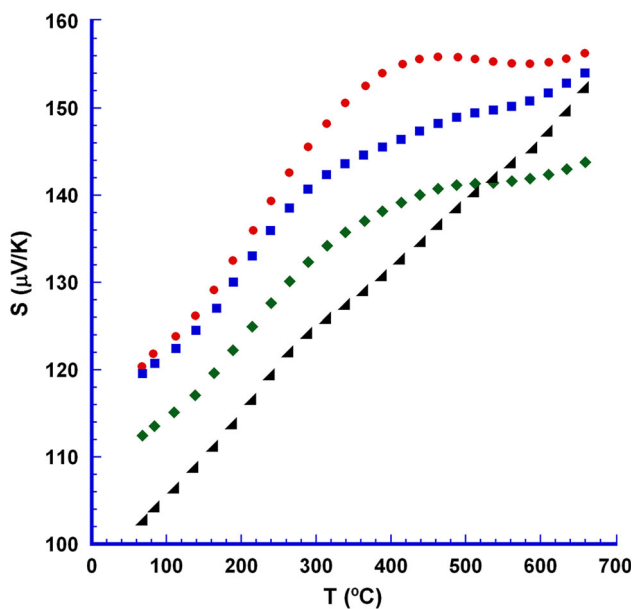


Fig. 5 Temperature dependence of Seebeck coefficient for as-grown $\text{Bi}_2\text{Ba}_2\text{Co}_2\text{O}_8$ samples with different Ag content: circle 0; square 1; diamond 3; and lower right triangle 5 wt%

easily seen in the plot, S is positive in the whole measured temperature range, indicating a conduction mechanism mainly governed by holes. At room temperature S values decrease with the Ag content. This evolution practically agrees with the measured room temperature electrical resistivity evolution, with the only exception of 5 wt% Ag samples, due their large Ag content which promotes the formation of large Ag particles, locally disturbing the solidification front avoiding the adequate TE phase formation (see Fig. 3). The general behaviour of the Ag-free samples is similar to the observed in previous works [33], and it is clearly modified when Ag is added. As a consequence, the maximum S values at room temperature are determined in Ag-free samples ($\sim 120 \mu\text{V/K}$), which is higher than the obtained in sintered materials (between 80 and $100 \mu\text{V/K}$) [11, 41–46], Ag doped samples ($105 \mu\text{V/K}$) [41], or single crystals ($95\text{--}110 \mu\text{V/K}$) [48, 49]. Moreover, they are comparable to the measured in textured materials ($115\text{--}145 \mu\text{V/K}$) [12, 33, 42, 47]. On the other hand, it is clear that all samples show higher S values at $650 \text{ }^\circ\text{C}$ than at room temperature. The maximum values ($\sim 160 \mu\text{V/K}$) measured in Ag-free samples, are still higher than the reported for sintered ($105\text{--}120 \mu\text{V/K}$) [11, 43, 46] and comparable to the obtained in textured materials ($145\text{--}185 \mu\text{V/K}$) [12, 33, 47]. The high S values found in these as-grown materials are in agreement with previous works which showed that LFZ processing of these materials generates oxygen vacancies in a larger content than in bulk sintered samples [50]. As a consequence of the necessary reduction of Co^{4+} to Co^{3+} , the holes concentration

is decreased, leading to an increase of S [51]. It has already been evidenced that, when sintering under reducing atmosphere, the misfit phase $[\text{Ca}_2\text{CoO}_3][\text{CoO}_2]_{1.62}$ is not oxygen stoichiometric but contains considerable amounts of oxygen vacancies [52] and, as a consequence, similar behaviour should be expected in these as-grown samples.

The PF evolution with temperature has been determined from the electrical resistivity and Seebeck coefficient data, for all samples, and displayed in Fig. 6. As it can be clearly seen in the graph, no evident changes are produced for small Ag content (1 wt%) while PF reaches the maximum values in the whole measured temperature range for the 3 wt% Ag. Further Ag addition clearly decreases PF values, being in a clear agreement with the microstructural observations. Moreover, the PF evolution with Ag content clearly points out that the electrical resistivity variations in these samples possess much higher relevance than Seebeck coefficient ones. The maximum values obtained at room temperature ($0.055 \text{ mW/K}^2\text{m}$ in 3 wt% Ag samples) is much higher than the reported in pure or Ag-doped sintered materials (between 0.001 and $0.035 \text{ mW/K}^2\text{m}$) [11, 41–46], and comparable to the obtained in textured materials ($0.010\text{--}0.15 \text{ mW/K}^2\text{m}$) [12, 33, 42, 47]. On the other hand, in spite of the improvement induced by Ag addition, these maximum values are still far from the obtained in single crystals ($0.2\text{--}0.3 \text{ mW/K}^2\text{m}$) [48, 49].

Other general feature observed in Fig. 6 is that PF values are quasilinearly increased when temperature is raised, reaching their maximum measured values at $650 \text{ }^\circ\text{C}$. At this temperature, the highest determined values ($0.18 \text{ mW/K}^2\text{m}$ for the 3 wt% Ag samples) are much higher than the

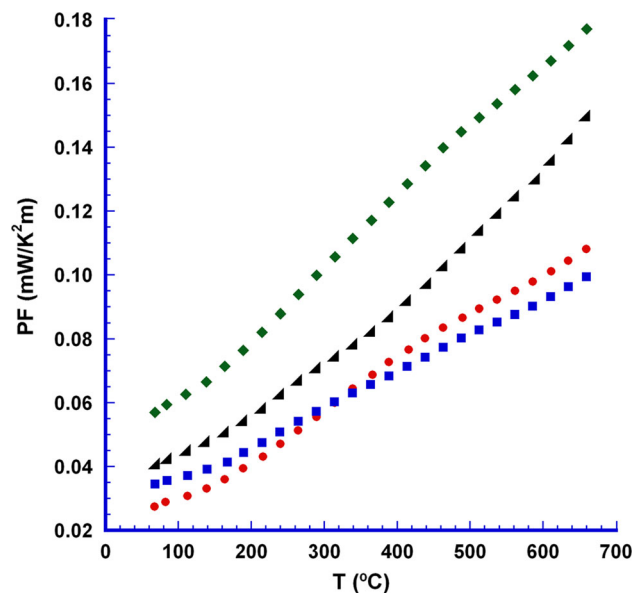


Fig. 6 Temperature dependence of PF for as-grown $\text{Bi}_2\text{Ba}_2\text{Co}_2\text{O}_8$ samples with different Ag content: circle 0; square 1; diamond 3; and lower right triangle 5 wt%

obtained in sintered materials ($0.013\text{--}0.040\text{ mW/K}^2\text{m}$) [11, 43, 46]. Furthermore, they are slightly higher than the best reported in laser textured materials grown at similar rates ($0.04\text{--}0.17\text{ mW/K}^2\text{m}$) [33, 47], but lower than the obtained in LFZ textured samples at very low growth rates ($0.40\text{ mW/K}^2\text{m}$ for 5 mm/h grown samples) [12].

From all these data, it can be easily deduced that Ag addition to $\text{Bi}_2\text{Ba}_2\text{Co}_2\text{O}_8$ LFZ textured materials lead to enhanced thermoelectric properties. Despite these improvements, their thermoelectric properties are still far from the values measured in single crystals. Among the factors which are limiting the raise in their properties, the high amount of secondary phases and the typical high oxygen vacancies produced when the materials are textured through the LFZ, can be highlighted. The high amount of secondary phases is produced by the incongruent melting found in these and similar materials [40, 47, 53] while the oxygen vacancies are due to the relatively rapid solidification of the melt, as previously reported [50]. On the other hand, it has been found that annealing processes performed on the as-grown textured samples, are very useful in order to palliate the inconveniences previously mentioned. As a consequence, the as-grown samples were subjected to an optimal thermal treatment consisting in one step heating at $750\text{ }^\circ\text{C}$ for 24 h (experimentally determined), followed by slow furnace cooling.

3.2 Annealed samples

After annealing, powdered samples were characterized through XRD, and the obtained patterns are displayed (from 5° to 40° for clarity) in Fig. 7. At a first sight, it is very clear that the amount of secondary phases has been drastically reduced by annealing and, when increasing Ag content, further decrease seems to be produced. Similarly to the observations made in the as-grown samples (see Fig. 1), most of the peaks correspond to the misfit cobaltite $\text{Bi}_2\text{Ba}_2\text{Co}_2\text{O}_8$ phase (indicated by their diffraction planes in Fig. 7a) [11], the peaks marked with a asterisk can be associated to a Bi–Ba–O solid solution with P121/n1 space group [37], while the one shown by hashtag in Fig. 7d corresponds to the (111) plane of metallic Ag [38]. This is a clear indication that annealing is not modifying the Ag particles composition and they are kept in metallic state.

These observed modifications have been confirmed by SEM observations performed on longitudinal polished sections of samples. The typical microstructures produced by the thermal treatment are illustrated in Fig. 8, where representative micrographs of all samples are presented. At a first sight, it can be clearly observed that the amount of secondary phases has been drastically reduced without evident modification in the grains orientation. Moreover, when studying these micrographs in detail, it has been

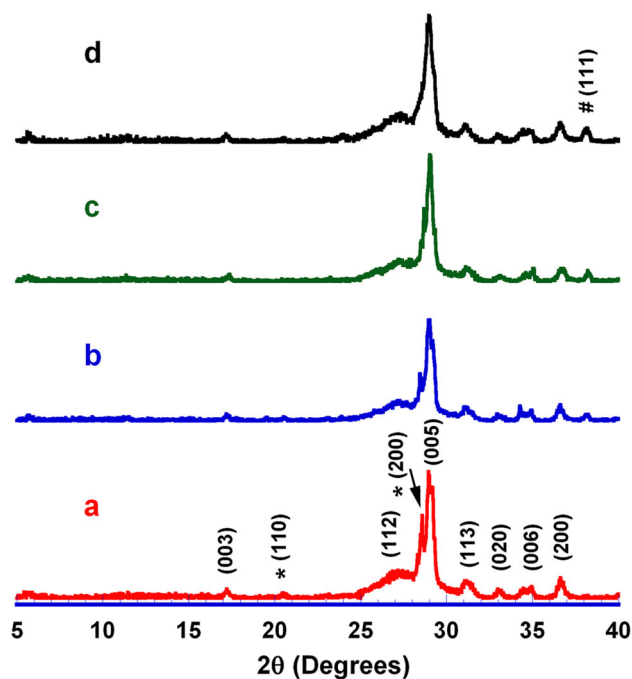


Fig. 7 Powder XRD diagrams for the annealed $\text{Bi}_2\text{Ba}_2\text{Co}_2\text{O}_8$ textured samples, with *a* 0; *b* 1; *c* 3; and *d* 5 wt% Ag. Crystallographic planes have been indicated for the $\text{Bi}_2\text{Ba}_2\text{Co}_2\text{O}_8$ phase. Asterisk corresponds to a Bi–Ba–O solid solution while the hashtag indicates the metallic Ag

found that all samples are formed by three main contrasts (numbered in the figure for clarity). All these contrasts have been associated through EDS analysis to different phases. Grey contrast (#1) corresponds to the $\text{Bi}_2\text{Ba}_2\text{Co}_2\text{O}_8$ phase, light grey (#2) to $\text{Bi}_3\text{Ba}_2\text{O}_7$, and dark grey (#3) to BaO. All these phases are the same identified in the as-grown samples, while the BaCo_2O_z one has disappeared after the thermal treatment. On the other hand, similarly to the observations in the as-grown samples, all the Ag containing ones show a grey contrast (#4, very similar to the #1) identified as metallic Ag particles with rounded shape, clearly confirming that Ag is kept in metallic state even after the thermal treatments, in agreement with the observations performed in a very close thermoelectric system [39]. Moreover, from these images, it is clear that the porosity is negligible in the textured annealed materials. In order to confirm this point, density of the different samples has been determined using the Archimedes method in, at least, four samples of each composition. The obtained results have been around 95 % of the theoretical one (taking into account a theoretical density of 7.20 g/cm^3 for the $\text{Bi}_2\text{Ba}_2\text{Co}_2\text{O}_8$ phase, and 10.49 g/cm^3 for Ag) in all cases.

In order to determine the effect produced by the annealing procedure in the electrical properties of these materials, the variation of electrical resistivity with

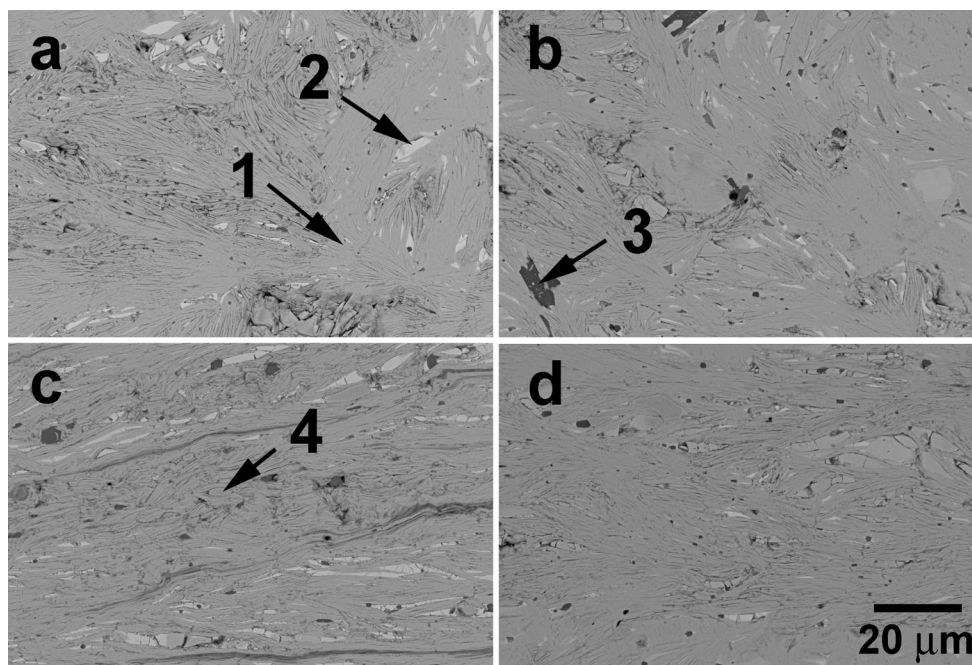


Fig. 8 SEM micrographs performed on longitudinal polished annealed $\text{Bi}_2\text{Ba}_2\text{Co}_2\text{O}_8$ textured samples with different Ag content: *a* 0; *b* 1; *c* 3; and *d* 5 wt%. The numbers indicate different phases: (#1) $\text{Bi}_2\text{Ba}_2\text{Co}_2\text{O}_8$; (#2) Bi–Ba–O solid solution; (#3) BaO; and (#4) metallic Ag

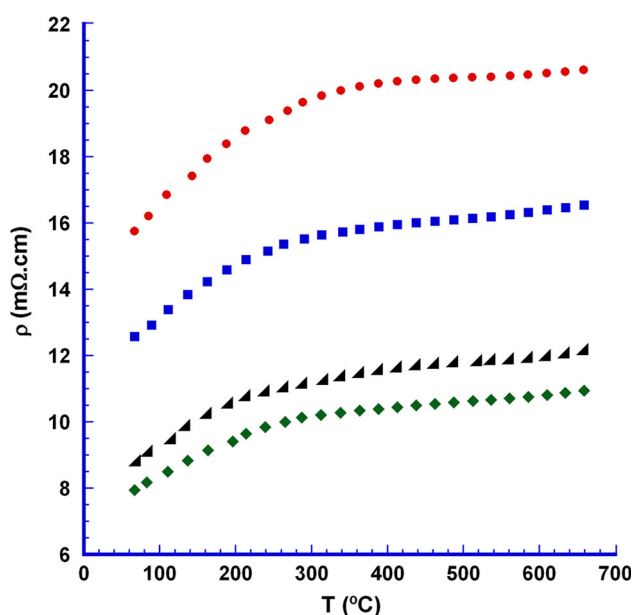


Fig. 9 Temperature dependence of the electrical resistivity for annealed $\text{Bi}_2\text{Ba}_2\text{Co}_2\text{O}_8$ textured samples with different Ag content: circle 0; square 1; diamond 3; and lower right triangle 5 wt%. The inset shows a large Ag particle in the outer zone of the 5 wt% Ag samples

temperature has been determined and displayed in Fig. 9. From these data, it is clear that electrical resistivity is drastically decreased when compared with the values obtained in the as-grown materials (see Fig. 4). This modification is in agreement with the decrease of

secondary phases, together with the reduction of oxygen vacancies produced in the LFZ process. These facts are associated to cations diffusion to produce the thermoelectric phase, as well as oxygen diffusion to the inner part of the rods during the annealing process. Moreover, it can also explain the different general behaviour observed in these samples, changing from a semiconducting-like, observed in the as-grown materials, to a metallic-like after annealing, clearly indicating a higher charge carrier concentration corroborating the higher oxygen content in the thermoelectric phase. On the other hand, it is very clear that Ag addition decreases electrical resistivity, compared with the values determined in Ag-free samples. Moreover, when considering Ag containing samples, electrical resistivity is reduced until 3 wt%, increased for further Ag content. This evolution is in agreement with previous works which showed that the optimum Ag content in these samples was very small (1–3 wt%) [27, 34]. On the other hand, the electrical resistivity raise observed in the 5 wt% Ag samples can be explained with the previous observations of large Ag spherical particles in the outer part of the rods, in agreement with previous works [54], when the Ag content is high. These large particles are responsible of an important local misalignment of grains and, consequently, raising electrical resistivities due to their anisotropic nature. In order to confirm the presence of these large Ag particles, general longitudinal polished sections of these samples were studied using FESEM and a representative image is shown in Fig. 10, where a large Ag particle has been

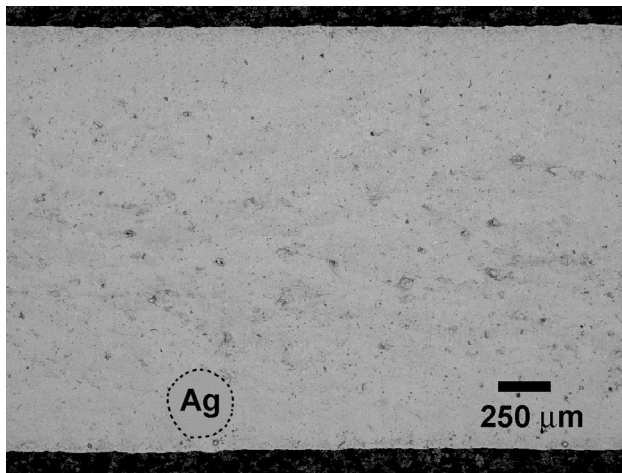


Fig. 10 General SEM micrograph performed in a longitudinal polished annealed $\text{Bi}_2\text{Ba}_2\text{Co}_2\text{O}_8 + 5 \text{ wt}\%$ Ag textured sample. The black dotted line surrounds a large Ag particle

identified by a circle for clarity. As it can be clearly observed in this image, nearly no secondary phases can be observed after the annealing process. Moreover, the Ag particle size is slightly lower than the observed in the as-grown samples (see Fig. 3), probably due to the Ag diffusion along the bulk samples during the annealing procedure. In spite of this diffusion process, the size of these Ag particles is still higher than $250 \mu\text{m}$ in diameter, being a clear obstacle for a high electrical conductivity.

When considering the obtained values at room temperature, the lowest ones ($\sim 8 \text{ m}\Omega \text{ cm}$) are lower than the measured in as-grown samples ($22 \text{ m}\Omega \text{ cm}$), or textured $\text{Bi}_2\text{Ba}_2\text{Co}_2\text{O}_8$ materials ($10\text{--}250 \text{ m}\Omega \text{ cm}$) [12, 33, 42, 47], and relatively close to the values determined in single crystals along the ab plane ($4 \text{ m}\Omega \text{ cm}$) [48, 49]. On the other hand, the high temperature values ($\sim 11 \text{ m}\Omega \text{ cm}$ at $650 \text{ }^\circ\text{C}$), are clearly lower than the ones found in $\text{Bi}_2\text{Ba}_2\text{Co}_2\text{O}_8$ sintered materials ($33 \text{ m}\Omega \text{ cm}$) [11, 43] and comparable with the obtained in $\text{Bi}_2\text{Ba}_2\text{Co}_2\text{O}_8$ textured samples (between 8.5 and $50 \text{ m}\Omega \text{ cm}$) [12, 33, 47].

Figure 11 displays the variation of the Seebeck coefficient as a function of temperature for all the samples. As it can be observed, all samples possess, approximately, the same S values in the whole measured temperature range, especially in the case of the Ag containing ones. Moreover, the nearly linear increase of S with temperature can be associated with a metal or degenerated semiconductor typical behaviour when the variation of carrier concentration, effective mass, and Fermi level with temperature are negligible. This behaviour is in a clear agreement with the metallic character of samples found in the electrical resistivity measurements. At first sight, the most remarkable difference can be found in the modification in the Seebeck coefficient response with temperature between as-

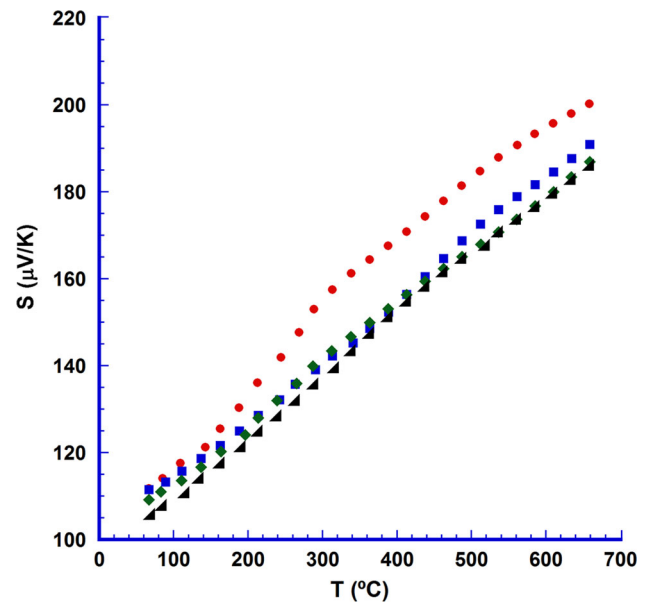


Fig. 11 Temperature dependence of Seebeck coefficient for annealed $\text{Bi}_2\text{Ba}_2\text{Co}_2\text{O}_8$ textured samples with different Ag content: *circle* 0; *square* 1; *diamond* 3; and *lower right triangle* 5 wt%

grown and annealed samples (see Figs. 5, 10). This effect is associated to the different oxygen content between the two types of samples. Moreover, the best Seebeck coefficient values at room temperature for the annealed samples (around $110 \mu\text{V/K}$) are slightly lower than the highest obtained in the as-grown ones (about $120 \mu\text{V K}^{-1}$) which clearly agree with the increase in oxygen in the structure produced by the annealing process, previously discussed. In any case, these high S values in the annealed samples are higher than the obtained in sintered materials (between 80 and $100 \mu\text{V/K}$) [11, 41–46], or Ag doped samples ($105 \mu\text{V/K}$) [41], and comparable to the measured in single crystals ($95\text{--}110 \mu\text{V/K}$) [48, 49]. On the other hand, they are clearly lower than the measured in textured materials ($115\text{--}145 \mu\text{V/K}$) [12, 33, 42, 47]. On the other hand, at $650 \text{ }^\circ\text{C}$, the maximum values ($\sim 200 \mu\text{V/K}$ in Ag-free samples, and $\sim 190 \mu\text{V/K}$ in Ag containing ones) are clearly higher than the reported in sintered ($105\text{--}120 \mu\text{V/K}$) [11, 43, 46], and slightly higher than the obtained in textured materials ($145\text{--}185 \mu\text{V/K}$) [12, 33, 47] being, in the best of our knowledge, the highest ever reported in this compound.

From the electrical resistivity and Seebeck coefficient data, PF has been calculated and presented, as a function of temperature, in Fig. 12. As it can be clearly observed when comparing Figs. 6 and 12, a very important raise of PF is promoted by the annealing procedure due to the drastic decrease observed in the electrical resistivity values. In the case of the best values obtained in both cases (in the 3 wt% Ag samples), the improvement ranges from around three

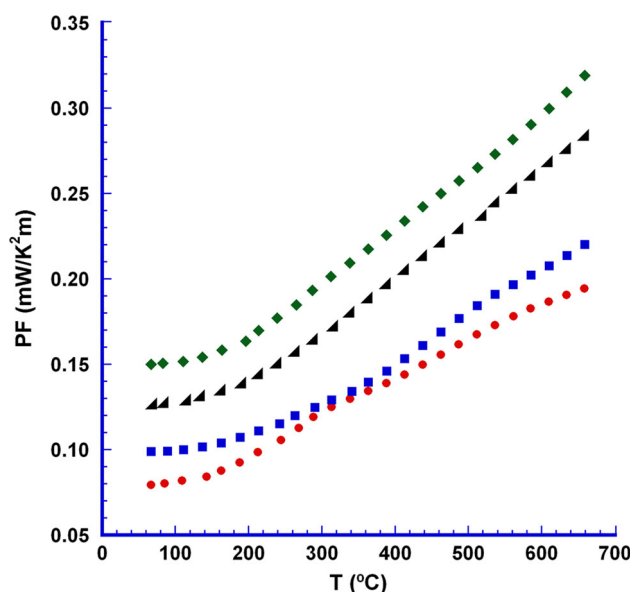


Fig. 12 Temperature dependence of PF for annealed $\text{Bi}_2\text{Ba}_2\text{Co}_2\text{O}_8$ textured samples with different Ag content: circle 0; square 1; diamond 3; and lower right triangle 5 wt%

times at room temperature, to nearly two times at 650 °C, clearly reflecting the larger amount of thermoelectric phase, together with its higher oxygen content, promoted by the annealing procedure. As a consequence, the highest PF values at room temperature (0.15 mW/K²m) are much higher than the reported in pure or Ag-doped sintered materials (between 0.001 and 0.035 mW/K²m) [11, 41–46], and comparable to the best obtained in textured materials (0.010–0.15 mW/K²m) [12, 33, 42, 47]. Moreover, these improvements induced by annealing lead to values closer to the obtained in single crystals (0.2–0.3 mW/K²m) [48, 49].

On the other hand, the maximum measured values are reached at 650 °C (0.32 mW/K²m for the 3 wt% Ag samples) which are again much higher than the obtained in sintered materials (0.013–0.040 mW/K²m) [11, 43, 46], or the best reported in laser textured materials grown at similar rates (0.04–0.17 mW/K²m) [33, 47], and close to the obtained in LFZ textured samples grown at very low rates (0.40 mW/K²m at 5 mm/h) [12]. These data clearly show the beneficial effect promoted by the combined effect of Ag addition and annealing in LFZ textured samples grown at relatively high rates.

4 Conclusions

This paper demonstrates that $\text{Bi}_2\text{Ba}_2\text{Co}_2\text{O}_8$ thermoelectric materials with small Ag additions (0, 1, 3, and 5 wt%) can be directionally grown by the laser floating zone method. It has been found that Ag addition leads to improved

thermoelectric performances. Moreover, annealing process further improves their performances by decreasing the amount of secondary phases and raising the oxygen content in the thermoelectric phase. Microstructural analysis shows that 3 wt% Ag significantly improves the sample texture, reflected in the electrical resistivity decrease without drastic modification of Seebeck coefficient. As a consequence of these effects, PF has been significantly improved when compared with Ag-free samples. The highest PF value has been reached at 650 °C in the 3 wt% Ag annealed samples (0.32 mW/K²m), which is close to the best reported values obtained in LFZ textured samples at very low rates (5 mm/h). These results clearly show that these textured materials can be regarded as very attractive candidates for practical energy generation applications.

Acknowledgments This research has been supported by the Spanish MINECO-FEDER (MAT2013-46505-C3-1-R). The authors wish to thank the Gobierno de Aragón and Fondo Social Europeo (Consolidated Research Groups T87 and T12) for financial support and to C. Gallego, and C. Estepa for their technical assistance. Authors would like to acknowledge the use of Servicio General de Apoyo a la Investigación-SAI, Universidad de Zaragoza.

References

1. D.M. Rowe, in *Thermoelectrics Handbook: Macro to Nano*, 1st edn., ed. by D.M. Rowe (CRC Press, Boca Raton, 2006), pp. 1–3–1–7
2. S. Sharma, V.K. Dwivedi, S.N. Pandit, *Int. J. Green Energy* **11**, 899 (2012)
3. M.H. Elsheikh, D.A. Shnawah, M.F.M. Sabri, S.B.M. Said, M.H. Hassan, M.B.A. Bashir, M. Mohamad, *Renew. Sustain. Energy Rev.* **30**, 337 (2014)
4. I. Terasaki, Y. Sasago, K. Uchinokura, *Phys. Rev. B* **56**, 12685 (1997)
5. Y. Huang, B. Zhao, J. Fang, R. Ang, Y. Sun, *J. Appl. Phys.* **110**, 123713 (2011)
6. A. Sotelo, G. Constantinescu, Sh Rasekh, M.A. Torres, J.C. Diez, M.A. Madre, *J. Eur. Ceram. Soc.* **32**, 2415 (2012)
7. N. Sun, S.T. Dong, B.B. Zhang, Y.B. Chen, J. Zhou, S.T. Zhang, Z.B. Gu, S.H. Yao, Y.F. Chen, *J. Appl. Phys.* **114**, 043705 (2013)
8. A. Sotelo, Sh Rasekh, M.A. Madre, E. Guilmeau, S. Marinell, J.C. Diez, *J. Eur. Ceram. Soc.* **31**, 1763 (2011)
9. K. Rubesova, T. Hlasek, V. Jakes, S. Huber, J. Hejtmanek, D. Sedmidubsky, *J. Eur. Ceram. Soc.* **35**, 525 (2014)
10. M.A. Madre, Sh Rasekh, J.C. Diez, A. Sotelo, *Mater. Lett.* **64**, 2566 (2010)
11. H. Hao, H. Yang, Y. Liu, X. Hu, *J. Mater. Sci. Technol.* **27**, 525 (2011)
12. G. Constantinescu, Sh Rasekh, M.A. Torres, M.A. Madre, J.C. Diez, A. Sotelo, *Scr. Mater.* **68**, 75 (2013)
13. A. Maignan, S. Hebert, M. Hervieu, C. Michel, D. Pelloquin, D. Khomskii, *J. Phys. Condens. Matter* **15**, 2711 (2003)
14. H. Itahara, C. Xia, J. Sugiyama, T. Tani, *J. Mater. Chem.* **14**, 61 (2004)
15. H. Wang, X. Sun, X. Yan, D. Huo, X. Li, J.-G. Li, X.D. Ding, *J. Alloys Compd.* **582**, 294 (2014)
16. D. Kenfaui, B. Lenoir, D. Chateigner, B. Ouladdiaf, M. Gomina, J.G. Noudem, *J. Eur. Ceram. Soc.* **32**, 2405 (2012)

17. N.Y. Wu, T.C. Holgate, N.V. Nong, N. Pryds, S. Linderoth, J. Eur. Ceram. Soc. **34**, 925 (2014)
18. J.G. Noudem, D. Kenfaui, D. Chateigner, M. Gomina, Scr. Mater. **66**, 258 (2012)
19. J.C. Diez, E. Guilmeau, M.A. Madre, S. Marinell, S. Lemmonier, A. Sotelo, Solid State Ionics **180**, 827 (2009)
20. K.R. Reddy, M. Hassan, V.G. Gomes, Appl. Catal. A **489**, 1 (2015)
21. C.R. Chandraiahgari, G. de Bellis, P. Ballirano, S.K. Balijepalli, S. Kaciulis, L. Caneve, F. Sarto, M.S. Sarto, RSC Adv. **5**, 49861 (2015)
22. A.M. Showkat, Y.-P. Zhang, M.S. Kim, A.I. Gopalan, K.R. Reddy, K.-P. Lee, Bull. Korean Chem. Soc. **28**, 1885 (2007)
23. K.R. Reddy, V.G. Gomes, M. Hassan, Mater. Res. Express **1**, 015012 (2014)
24. K.R. Reddy, B.C. Sin, C.H. Yoo, W. Park, K.S. Ryu, J.-S. Lee, D. Sohn, Y. Lee, Scr. Mater. **58**, 1010 (2008)
25. N.M. Ferreira, Sh Rasekh, F.M. Costa, M.A. Madre, A. Sotelo, J.C. Diez, M.A. Torres, Mater. Lett. **83**, 144 (2012)
26. M. Hassan, E. Haque, K.R. Reddy, A.I. Minett, J. Chen, V.G. Gomes, Nanoscale **6**, 11988 (2014)
27. A. Sotelo, M.A. Torres, G. Constantinescu, Sh Rasekh, J.C. Diez, M.A. Madre, J. Eur. Ceram. Soc. **32**, 3745 (2012)
28. M. Ito, D. Furumoto, J. Alloys Compd. **450**, 517 (2008)
29. S. Wang, Z. Bai, H. Wang, Q. Lü, J. Wang, G. Fu, J. Alloys Compd. **554**, 254 (2013)
30. F. Kahraman, M.A. Madre, Sh Rasekh, C. Salvador, P. Bosque, M.A. Torres, J.C. Diez, A. Sotelo, J. Eur. Ceram. Soc. **35**, 3835 (2015)
31. A. Sotelo, M.A. Madre, Sh Rasekh, J.C. Diez, L.A. Angurel, Adv. Appl. Ceram. **108**, 285 (2009)
32. F.M. Costa, N.M. Ferreira, Sh Rasekh, A.J.S. Fernandes, M.A. Torres, M.A. Madre, J.C. Diez, A. Sotelo, Cryst. Growth Des. **15**, 2094 (2015)
33. Sh Rasekh, G. Constantinescu, M.A. Torres, M.A. Madre, J.C. Diez, A. Sotelo, Adv. Appl. Ceram. **111**, 490 (2012)
34. A. Sotelo, Sh Rasekh, G. Constantinescu, M.A. Torres, M.A. Madre, J.C. Diez, Ceram. Int. **39**, 1597 (2013)
35. M.F. Carrasco, F.M. Costa, R.F. Silva, F. Gimeno, A. Sotelo, M. Mora, J.C. Diez, L.A. Angurel, Phys. C **415**, 163 (2004)
36. Sh Rasekh, F.M. Costa, N.M. Ferreira, M.A. Torres, M.A. Madre, J.C. Diez, A. Sotelo, Mater. Des. **75**, 143 (2015)
37. Q.D. Zhou, Z.M. Zhang, B.J. Kennedy, C.J. Howard, K.S. Knight, Acta Cryst. B **62**, 537 (2006)
38. E. Jette, F. Foote, J. Chem. Phys. **3**, 605 (1935)
39. D. Flahaut, J. Allouche, A. Sotelo, Sh Rasekh, M.A. Torres, M.A. Madre, J.C. Diez, Acta Mater. **102**, 273 (2016)
40. M.A. Madre, F.M. Costa, N.M. Ferreira, A. Sotelo, M.A. Torres, G. Constantinescu, Sh Rasekh, J.C. Diez, J. Eur. Ceram. Soc. **33**, 1747 (2013)
41. R. Ang, Y.P. Sun, X. Luo, W.H. Song, J. Appl. Phys. **102**, 073721 (2007)
42. T. Motohashi, Y. Nonaka, K. Sakai, M. Karppinen, H. Yamauchi, J. Appl. Phys. **103**, 033705 (2008)
43. H. Hao, H. Yu, L. Zhao, Adv. Mater. Res. **228–229**, 804 (2011)
44. M. Hervieu, A. Maignan, C. Michel, V. Hardy, N. Creon, B. Raveau, Phys. Rev. B **67**, 045112 (2003)
45. K. Sakai, T. Motohashi, M. Karppinen, H. Yamauchi, Thin Solid Films **486**, 58 (2005)
46. K. Sakai, M. Karppinen, J.M. Chen, R.S. Liu, S. Sugihara, H. Yamauchi, Appl. Phys. Lett. **88**, 232102 (2006)
47. M.A. Madre, F.M. Costa, N.M. Ferreira, S.I.R. Costa, Sh Rasekh, M.A. Torres, J.C. Diez, V.S. Amaral, J.S. Amaral, A. Sotelo, J. Eur. Ceram. Soc. **36**, 67 (2016)
48. W. Kobayashi, S. Hebert, H. Muguerra, D. Grebille, D. Pelloquin, A. Maignan, *Proceedings ICT'07* (Piscataway, NJ, USA, IEEE, 2008), pp. 117–120
49. X.G. Luo, H. Chen, G.Y. Wang, G. Wu, T. Wu, L. Zhao, X.H. Chen, J. Phys. Condens. Matter **20**, 215221 (2008)
50. J.C. Diez, Sh Rasekh, M.A. Madre, E. Guilmeau, S. Marinell, A. Sotelo, J. Electron. Mater. **39**, 1601 (2010)
51. A. Maignan, D. Pelloquin, S. Hebert, Y. Klein, M. Hervieu, Bol. Soc. Esp. Ceram. **45**, 122 (2006)
52. M. Karppinen, H. Fjellvåg, T. Konno, Y. Morita, T. Motohashi, H. Yamauchi, Chem. Mater. **16**, 2790 (2004)
53. M.F. Carrasco, V.S. Amaral, R.F. Silva, J.M. Vieira, F.M. Costa, Appl. Surf. Sci. **252**, 4957 (2006)
54. A. Sotelo, M. Mora, M.A. Madre, J.C. Diez, L.A. Angurel, G.F. de la Fuente, J. Eur. Ceram. Soc. **25**, 2947 (2005)